Bioactive Materials 6 (2021) 312–325

Contents lists available at ScienceDirect

Bioactive Materials

journal homepage: http://www.keaipublishing.com/biomat

Reversing cold tumors to hot: An immunoadjuvant-functionalized metal-organic framework for multimodal imaging-guided synergistic photo-immunotherapy

Zhijin Fan[a,1], Hongxing Liu[b,1], Yaohua Xue[a], Jingyan Lin[c], Yu Fu[c], Zhaohua Xia[c], Dongming Pan[c], Jian Zhang[d,**], Kun Qiao[c,***], Zhenzhen Zhang[e], Yuhui Liao[a,*]

[a] Molecular Diagnosis and Treatment Center for Infectious Diseases, Dermatology Hospital, Southern Medical University, Guangzhou, 510091, China
[b] Department of Urology, Guangzhou Institute of Urology, Guangdong Key Laboratory of Urology, the First Affiliated Hospital of Guangzhou Medical University, Guangzhou Medical University, Guangzhou, Guangdong, 510230, China
[c] Department of Thoracic Surgery, Shenzhen Third People's Hospital, Shenzhen, 518110, China
[d] Department of Biomedical Engineering, School of Basic Medical Science, Guangzhou Medical University, Guangzhou, 511436, China
[e] Institute for Brain Research and Rehabilitation, South China Normal University, Guangzhou, 510631, China

ARTICLE INFO

Keywords:
Synergistic cancer photoimmunotherapy
Multimodal imaging
Metal-organic frameworks
CpG
Hot tumor

ABSTRACT

Immunotherapy assays using immunoadjuvants and tumor antigens could greatly increase the survival rates of patients with malignant tumors. As effective carriers, metal-organic frameworks (MOFs) have been widely utilized in cancer therapy due to their remarkable histocompatibility and low toxicity. Herein, we constructed a multimodal imaging-guided synergistic cancer photoimmunotherapy by employing a specific MOF (MIL101-NH_2) as the core carrier; the MOF was dual-dressed with photoacoustic and fluorescent signal donors (indocyanine green, ICG) and immune adjuvants (cytosine-phosphate-guanine sequence, CpG) and named ICG-CpG@MOF. This nanocarrier could passively target the tumor site through the EPR effect and achieve multimodal imaging (fluorescence, photoacoustic, photothermal and magnetic resonance imaging) of the tumor. Synergistic cancer photoimmunotherapy was achieved via simultaneous photodynamic and photothermal methods with 808 nm laser irradiation. ICG-CpG@MOF achieved the GSH-controlled release of immunoadjuvant into the tumor microenvironment. Furthermore, the released tumor-associated antigen along with CpG could induce the transformation of tumor cells from cold to hot by activating the immune system, which significantly enhanced tumor cytotoxicity and achieved high cure rates with minimal side-effects. This strategy utilizing multimodal imaging and synergistic cancer photoimmunotherapy provides a promising approach for the diagnosis and treatment of cancer.

1. Introductions

Malignant tumors have become the leading threat to public health due to their high morbidity and mortality, and effective treatment of advanced cancer remains a clinical challenge [1,2]. Radiotherapy and chemotherapy, conventional first-line treatments, are troubled by tumor recurrence and metastasis, because of the side effect and the serious injury of host's immunity [3]. Recently, immunotherapy for cancer treatment has emerged as a promising therapeutic modality for recurrent or metastasized cancer, as it converts cold tumors into hot tumors [4–7]. Immunotherapy aims to induce or expand the host's anticancer immune response, which can distinguish the subtle differences between cancerous cells and healthy cells. In recent years, great progress has been made in treating malignant tumors via activation of the host's immune system, targeted cellular therapeutics [8–12], immune checkpoint blockade [13–15], and therapeutic cancer vaccines [16–19].

Despite significant advances in cancer immunotherapy, there are

Peer review under responsibility of KeAi Communications Co., Ltd.
* Corresponding author.
** Corresponding author.
*** Corresponding author.
E-mail addresses: jianzhang@gzhmu.edu.cn (J. Zhang), szqiaokun@163.com (K. Qiao), liaoyh8@mail.sysu.edu.cn (Y. Liao).
[1] These authors contribute equally to this work.

https://doi.org/10.1016/j.bioactmat.2020.08.005
Received 5 June 2020; Received in revised form 6 August 2020; Accepted 6 August 2020

still limitations, such as individual differences, low response to treatment, and severe side effects. Therefore, it is highly desirable to improve the immune response rate and selectively destroy primary solid tumors and metastatic lesions. In recent years, immunotherapy combined with nanotechnology, defined as nanoimmunotherapy, has shown promising performance for cancer therapy [19–30]. Among these therapeutics, metal-organic frameworks (MOFs), as a crystal material, has been widely studied in biomedical field [31–37]. MOFs of nanosized iron carboxylate, especially MIL101(Fe), have attracted considerable attention due to their excellent biocompatibility and biodegradability [38–40]. MOFs were used as an effective nanocarrier in the context of drug delivery, targeted imaging and immune enhancement [41]. Zhang et al. reported that a MOF loaded with CpG oligonucleotides (CpG ODN), a Toll-like receptor 9 activator, could enhance the immune response and imaging [42]. Yang et al. found thata codelivery system for CpG ODN and a single tumor antigen based on anano MOFcould elicit a potent anti-tumor cellular immune response [43]. However, there are still many limitations of MOF-mediated immunotherapy. Among these approaches, the immunotherapy strategy of loading with tumor antigen cannot address the individual differences and tumor heterogeneity of patients. In addition, the strategy of in situ tumor immunity via loading with immune adjuvant lacks targeting and easily causes the systemic immune overreaction. Therefore, it is of great significance to develop precise immunotherapy guided by multimodal imaging.

In this study, we constructed a multimodal imaging-guided synergistic cancer photoimmunotherapy by employing MIL101-NH_2 dual-dressed with photoacoustic and fluorescent signal donors (indocyanine green, ICG) and immune adjuvants (CpG ODN) as the core carrier; this tool was named ICG-CpG@MOF (Scheme 1A). ICG has both photodynamic and photothermal effects under 808 nm laser irradiation. Herein, ICG has dual functions as a trigger for the nanoparticle to initiate light-mediated tumor therapy and as a tumor imaging contrast agent. This nanocarrier (ICG-CpG@MOF) can passively target tumors through enhanced permeability and retention (EPR), achieve multimodal imaging (fluorescence, photoacoustic, photothermal and MR imaging) of tumors, and simultaneouslyachieve light-actuated tumor therapy, including photodynamic and photothermal methods. After the nanoparticles entered the tumor cells via amplified macropinocytosis, the tumor cells could be killed by increased ROS accumulation when 808 nm laser irradiation was applied. Furthermore, ICG could directly destroy tumor cells and lead to tumor antigen release due to the photothermal effect of ICG. The released tumor-associated antigen along with CpG could induce the transformation of tumor cells from cold to hot by activating the immune system, which significantly enhanced tumor cytotoxicity and achieved high cure rates with minimal side effects (Scheme 1B). This strategy utilizing multimodal imaging-guided synergistic cancer photoimmunotherapy provides a promising approach for cancer diagnosis and treatment.

2. Results and discussion

2.1. Characterization of the functionalized MOF

We constructed a multimodal imaging-guided synergistic cancer photoimmunotherapy by employing MIL101-NH_2 dual-dressed with photoacoustic and fluorescent signal donors (indocyanine green, ICG) and immune adjuvants (CpG ODN) as the core carrier. This platform was named ICG-CpG@MOF. Characterization of ICG-CpG@MOF was first executed to verify the feasibility of the construction route. The TEM (transmission electron microscope) and SEM (scanning electron microscope) results in Fig. 1A and B demonstrated that MIL-101(NH_2) had a particle size of approximately 150 nm, and its particle size increased after co-loading of ICG and CpG (Fig. 1C). Then, the feasibility of ICG-CpG@MOF construction was investigated by atomic spectrum analysis. The TEM elemental maps (Fig. 1D) showed the distribution of C, N, P, S, and Fe on the same particle, which can be regarded as proof of the co-occurrence of ICG (containing sulfur) and CpG (containing

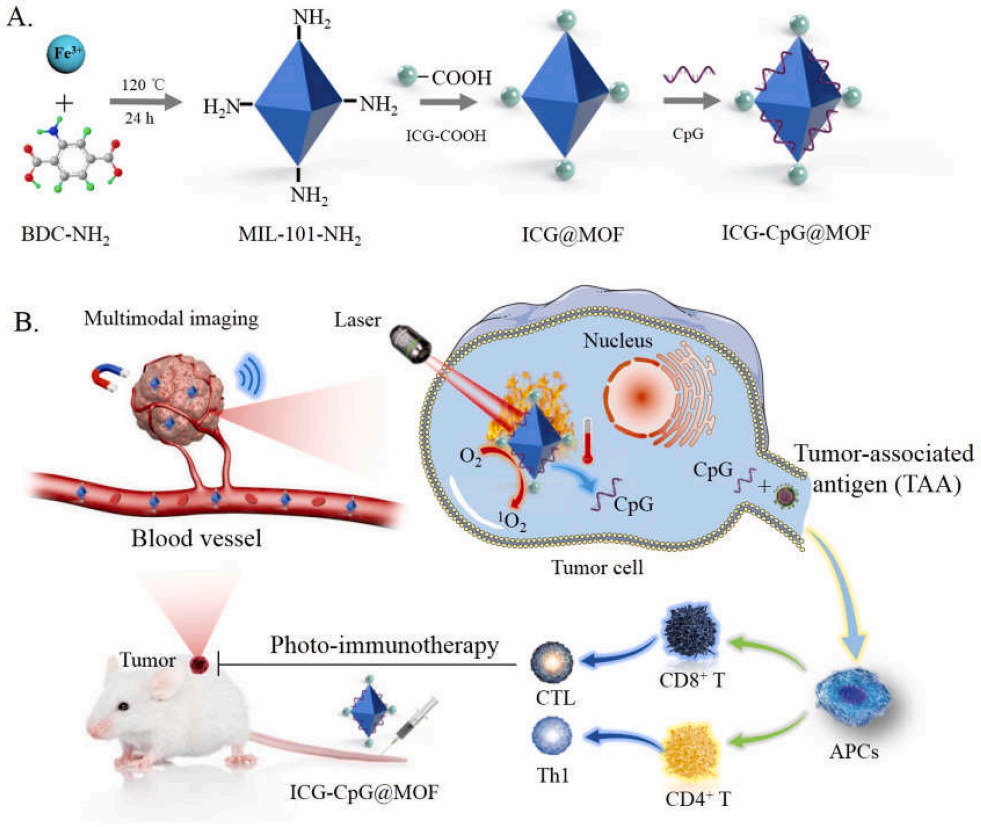

Scheme 1. Schematic illustration for A. Synthesis of ICG-CpG@MOF and **B.** Mechanism of multimodality imaging (photoacoustic, nuclear magnetic, fluorescence imaging) guided synergistic cancer photo-immunotherapy. MIL101-NH_2 is synthesized by heating the mixture of $FeCl_3$ and 2-amino-terephthalic acid (NH_2-BDC). The carboxyl-activated ICG was then connected to the amino of MIL101-NH_2 through the formation of amido bond. CpG was bound to MIL101-NH_2 by the effect of the porous and electrostatic adsorption. ICG-CpG@MOF enriched in tumor tissues through the EPR effect, and photoimmunotherapy was activated by 808 nm laser.

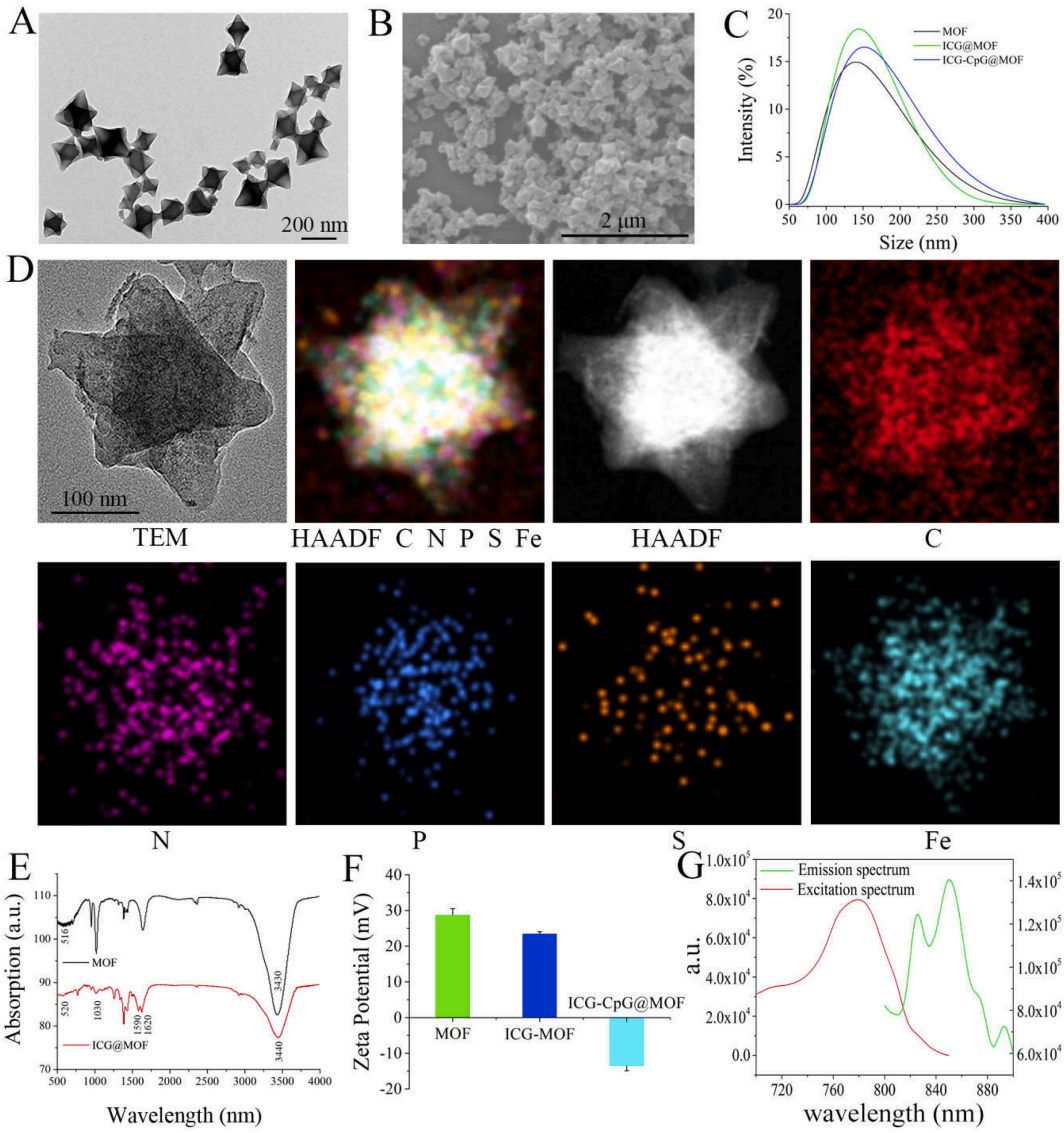

Fig. 1. Characterization of functionalized MOF. A. Morphology of MIL101-NH_2 was observed by TEM. **B.** Morphology of MOF was observed by SEM. **C.** Particle size change before and after modification of the MOF. **D.** Bright-field TEM image of ICG-CpG@MOF and relevant elemental mappings of C K edge, N K edge, P K edge, S K edge, and Fe K edge signals. **E.** Fourier transform infrared spectroscopy (FT-IR) for ICG-MOF. **F.** Zeta potential change before and after modification of MOF. **G.** Excitation and emission of ICG-CpG@ MOF.

phosphorus). These results were further confirmed by fourier transform infrared spectroscopy. As shown in Fig. 1E, the obvious stretching vibrations of carbonyl at 1620 cm^{-1} verified the conjugation of ICG. Additionally, as shown in Fig. 1F, the gradual decrease in the zeta potential of the MOFs, also indicated the loading of ICG and CpG ODN. We also detected the excitation and emission spectra of ICG-CpG@ MOF. The experimental results are shown in Fig. 1G. The excitation wavelength of the nanoparticles was 700–820 nm, and the fluorescence emission wavelength was 810–880 nm. The results of the UV spectrum comparison of MIL101-NH_2 and ICG-MIL101-NH_2 were consistent with the above results (Fig. S1). Thus, the feasibility of the construction route of ICG-CpG@MOF was verified.

To determine the loading efficiency of CpG ODN, 65 μg of CpG ODN was coincubated with 1 mg of ICG-MIL101-NH_2. After loading, the content of free CpG ODN in the supernatant was measured to be approximately 15 μg. The loading efficiency was calculated to be approximately 76% (Fig. S2). We also measured the release efficiency after GSH triggering, but the products of MOF degradation had an impact on DNA measurement, and the value we measured was significantly higher than the loading amount, with an A260/280 value of 2.75. For this reason, agarose gel electrophoresis was used to measure the nucleic acid content in each component, and the loading efficiency and release efficiency were calculated through grayscale analysis (Fig. S3). The loading efficiency results obtained by the two methods were consistent. As a mesoporous material, MIL101-NH_2 can efficiently adsorb molecules with diameters smaller than its pore diameters. For this reason, the aperture distribution of the MIL101-NH_2 was measured by N_2adsorption-desorption experiments, as shown in Fig. S4, with an average pore size of 2.8 nm. As shown in Fig. S5, the adsorption value of the material in the low-pressure area increased rapidly and there was a corresponding plateau period, indicating that the material had a microporous structure. The absence of an adsorption equilibrium in the high pressure region indicates that the material has a large pore structure. These results were consistent with the aperture distribution data. We speculated that CpG ODN could adsorbed to the interior of the MOF through the microporous structure and the CpG ODN could be released only after the MOF was decomposed. Then, we tested the response of the material to glutathione (GSH). One milligram of MOF was

added to a glutathione solution at different concentrations and incubated for 6 h, and then the change in particle size for each group was measured. As shown in Fig. S6, glutathione promoted a decrease in MOF particle size in a concentration-dependent manner. When the concentration reaches 100 μM, the particle size of the MOF tends to zero. The response of MOF to GSH can also be observed through color changes. With the increase of GSH concentration, the color of MOF becomes lighter (Fig. S7). The above results showed that the MOF had reduced responsiveness and could degrade and release CpG in the tumor microenvironment. We also tested the stability of MOF in different liquid environments. As shown in Fig. S8, the MOF was abnormally stable in PBS and DMEM, with no significant change in particle size within 24 h. However, in fetal bovine serum (FBS) or DMEM mixed with 10% FBS, the particle size of MOF gradually decreased with increasing time. These results indicate that MIL101-NH_2 is biodegradable. The materials have good biocompatibility.

2.2. Internalization of functionalized MOF in tumor cells

To determine whether the functionalized MOF without a targeted tag can be internalized by tumor cells, fluorescein isothiocyanate (FITC) was loaded on ICG-CpG@MOF (FITC-ICG-CpG@MOF) to evaluate its internalization efficiency in tumor cells. After the fluorescence-labeled MOF was incubated with 4T1 cells for a period of time (Fig. 2A, **B and S9**), punctate distribution of fluorescence in the cells could be observed, and the fluorescence intensity increased with increasing time, suggesting that the internalization of the MOF was time dependent. This phenomenon does not depend on specific receptors. Specifically, the material is adsorbed to the surface of tumor cells due to its porous and electrostatic nature and then internalized by tumor cells via endocytosis or macropinocytosis. We found that the macropinocytosis inhibitor EIPA significantly inhibited the internalization of ICG-CpG@MOF (Fig. 2A). It has been reported that tumor cells are in a unique state of hunger, and pinocytosis is significantly enhanced in these cells [44]. This will give the ICG-CpG@MOF the properties of passive tumor targeting.

2.3. Photothermal and photodynamic therapeutic activities of the functionalized MOF

To evaluate the performance of ICG-CpG@MOF as a photothermal agent in aqueous solution, the temperature variation of ICG-CpG@MOF was recorded at intervals after irradiation with NIR light (Fig. 3A and B). These results showed that the temperature of ICG-CpG@MOF increased sharply and reached equilibrium within 5 min after irradiation with an 808 nm laser. These results are consistent with the photothermal effect of ICG that was reported in other studies [45]. In addition, with increasing ICG-CpG@MOF concentration and laser power, the rate of temperature increase was proportionally improved (Fig. 3B, Fig. S10). Besides, the photothermal effects of ICG-CpG@MOF can be effectively repeated with the switch of the 808 nm laser (Fig. 3C).

To verify the photodynamic effect, a probe for reactive oxygen species (2′,7′-dichlorofluorescin diacetate, DCFH-DA) was incubated with the cells in advance, and the changes in fluorescence intensity were detected by fluorescence microscopy and flow cytometry immediately after laser irradiation. As shown in Fig. 3D, laser irradiation alone slightly increased intracellular ROS levels. However, the fluorescence intensity of cells incubated with ICG-CpG@MOF was significantly enhanced after laser irradiation. The same results were obtained by flow cytometry (Fig. 3E). The effects of laser irradiation on the production of reactive oxygen species in cells have been discussed in previous studies [46], but the phenomenon is not significant. Thus, ICG-CpG@MOF is the main reason for the increase of reactive oxygen species after laser irradiation.

2.4. Killing effect of tumor cells with ICG-CpG@MOF

To determine the safety of the ICG-CpG@MOF, cells were cocultured with 0–50 nM MOF for 48 h, and a CCK8 assay was used to measure cell activity. The results revealed no direct cytotoxic effects of ICG-CpG@MOF at 50 nM (Fig. S11). The optimal concentration which used to detect the cell activity after 1.5 W/cm^2 808 nm laser irradiation was selected as 20 nM in the following experiments. It can be seen from Fig. S12, laser irradiation alone had little effect on cell viability, while cells incubated with ICG-CpG@MOF exhibited significantly reduced cell viability after light exposure. This phenomenon may be attributed to the photothermal and photodynamic effects of ICG. Cell death was detected by flow cytometry apoptosis detection and Hoechst fluorescence staining. Annexin V/PI double staining showed that ICG-CpG@MOF did not induce apoptosis, but apoptosis occurred when an additional laser was used (Fig. 3F). The statistical results showed that laser irradiation after ICG-CpG@MOF treatment could trigger apoptosis of 70% of tumor cells, with a significant difference compared with the control group (Fig. S13). As shown in Fig. 3G, ICG-CpG@MOF resulted in cell death and peeling after laser treatment. We found that a laser dose of 1 W/cm^2 is not enough to make the cells peel off. However, there is still a large amount of cell death, which may be attributed to the photodynamic effect of ICG.

2.5. Effects of ICG-CpG@MOF on immune cells

As reported in previous research, nanoparticles can be taken up by mononuclear macrophages *in vivo* [47]. Thus, we examined the effect of ICG-CpG@MOF on primary peritoneal macrophage differentiation in mice. As shown in Fig. 4A, B and S14, CpG promoted the expression of CD80 (a membrane antigen necessary for T lymphocyte activation) in macrophages. CD11c expression was also increased. Moreover, ICG-CpG@MOF has a stronger activation effect on macrophages. This result may be attributed to the fact that the MOF promotes the internalization of CpG in macrophages. Moreover, the immune response was examined after ICG-CpG@MOF was added. We isolated the spleen cells and administered different stimuli (Fig. 4C and D and **4E)**, and then the differentiation of suspended T cells and adherent cells was detected. The results in Fig. 4C, D and S15 indicated that the CpG treatment promoted the expression of CD80 and CD11c in adherent cells from the spleen, while 4T1 cells inhibited the expression of CD80 and CD11c. After 4T1 cells were killed by ICG-CpG@MOF with laser irradiation and the remnants were cocultured with spleen cells, the expression of CD80 and CD11c in adherent cells was significantly increased. The differentiation of T cells was also verified by flow cytometry. As shown in Fig. 4E and Fig. S16, when the remnants after photothermal treatment were cocultured with spleen cells, CD4 and CD8 expression was significantly changed, and CD8 expression was significantly enhanced. These results indicated that the ICG-CpG@MOF nanoplatform could integrate photodynamic therapy (PDT), photothermal therapy (PTT) and GSH triggered immune adjuvant release to act as an in situ tumor vaccine, which could generate excellent immune activation effects. More importantly, after ICG-CpG@MOF treatment, macrophages differentiated into M1-type cells, and T cells were transformed into CD8-positive cells, both of which are considered major components of antitumor immunity.

Previous studies have shown that M1-type macrophages can inhibit tumor growth [48]. CD80 is a typical M1-type marker, so we tested the inhibitory effect of stimulated macrophages on tumor cells. The culture medium of the CpG and ICG-CpG@MOF treatment groups inhibited the activity of tumor cells. Flow cytometry showed that medium from CpG- and ICG-CpG@MOF-activated macrophages could induce tumor cell apoptosis (Fig. 5A). The apoptosis rate in ICG-CpG@MOF treatment group was as high as 33.62%. This result was significantly higher than that of the control group and also higher than that of the free CpG group. This result may be due to the lower internalization efficiency of free CpG than that of ICG-CpG@MOF in macrophage. CCK8 assay were

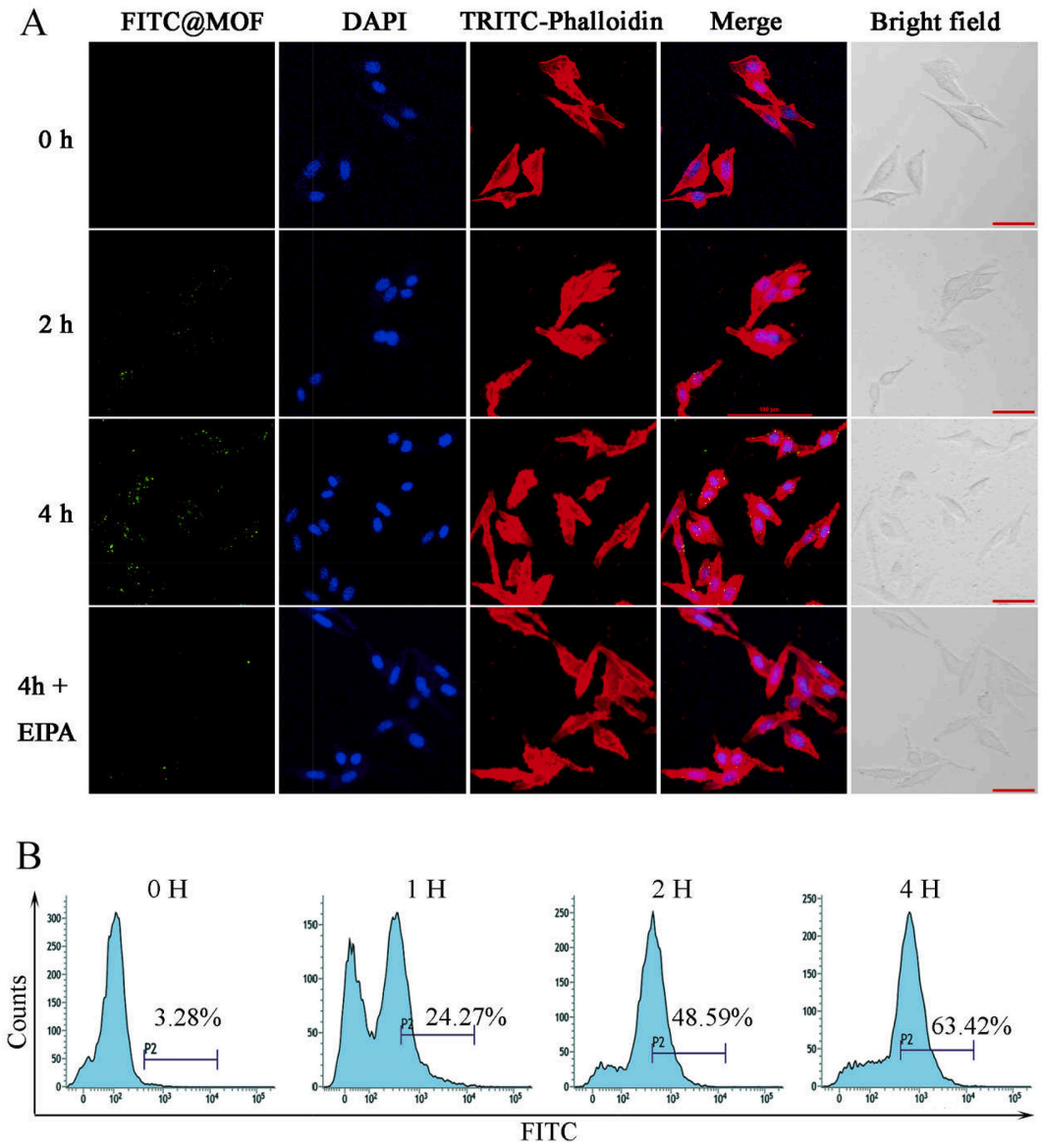

Fig. 2. Time-dependent internalization of FITC-labeled ICG-CpG@MOF by tumor cells. A. Confocal images to present the internalization of FITC-labeled ICG-CpG@MOF (20 μg/mL) by 4T1 breast cancer cells. EIPAis a macropinocytosis inhibitor. Scale bar: 50 μm. **B.** Internalization efficiency of ICG-CpG@MOF was detected by flow cytometry.

also detected. As shown in Fig. 5B, the ICG-CpG@MOF treatment group inhibited the activity of tumor cells. We then examined the response of T cells to 4T1 cells in different treatment groups (Fig. 5C). We found that T cells in the 4T1 treatment group and the 4T1 photothermal treatment group could bind to the surface of tumor cells, and the proportion of the 4T1 photothermal treatment group was significantly higher than that of the 4T1 treatment group. The killing effect of T cells on tumor cells was detected by flow cytometry. As shown in Fig. 5D, the remnants of photothermal therapy can activate the killing effect of T cells and cause more apoptosis of tumor cells. We also examined immune cytokine release of stimulated macrophages and T cells. The results showed that the levels of IL-6, IL-12p, TNF-α, and IFN-γ in the ICG-CpG@MOF treatment macrophage were higher than those in other groups (Fig. 5E), which were consistent with M1 macrophage maturation data in Fig. 4A. Furthermore, we also measured IL-4, IL-2, IFN-γ, and TNF-α levels by ELISA in T cells. The results showed that the levels of IL-2, IFN-γ, and TNF-α in the ICG-CpG@MOF + 4T1 + Laser group were the highest comparing with any other groups (Fig. 5F), which suggests that cellular immunity is activated. These results show that ICG-CpG@MOF can produce immune regulation effects after killing tumors.

2.6. Multimodal imaging in vivo

ICG-CpG@MOF was endowed with the functions of fluorescence, photoacoustic, photothermal, and nuclear magnetic resonance imaging. As shown in Fig. 6A, we evaluated the effect of fluorescence imaging after injection via the tail vein. The fluorescence signal could be detected at the tumor site from 1 h after injection, and the signal was enhanced within 24 h. At 48 h, the fluorescence intensity had decreased significantly. In order to comprehensively compare the distribution of ICG-CpG@MOF in various organs, we dissected the mice after anesthesia, and proceeded the analysis of fluorescence imaging for their organs at each time point. At 1 h after injection, fluorescence distribution appeared in liver, kidney, heart and lung. And the fluorescence intensity of liver was strongest and reached its maximum at 3 h after injection. The fluorescence intensity in the lung also reached its maximum at this time and then decreased significantly. At 6 h, the

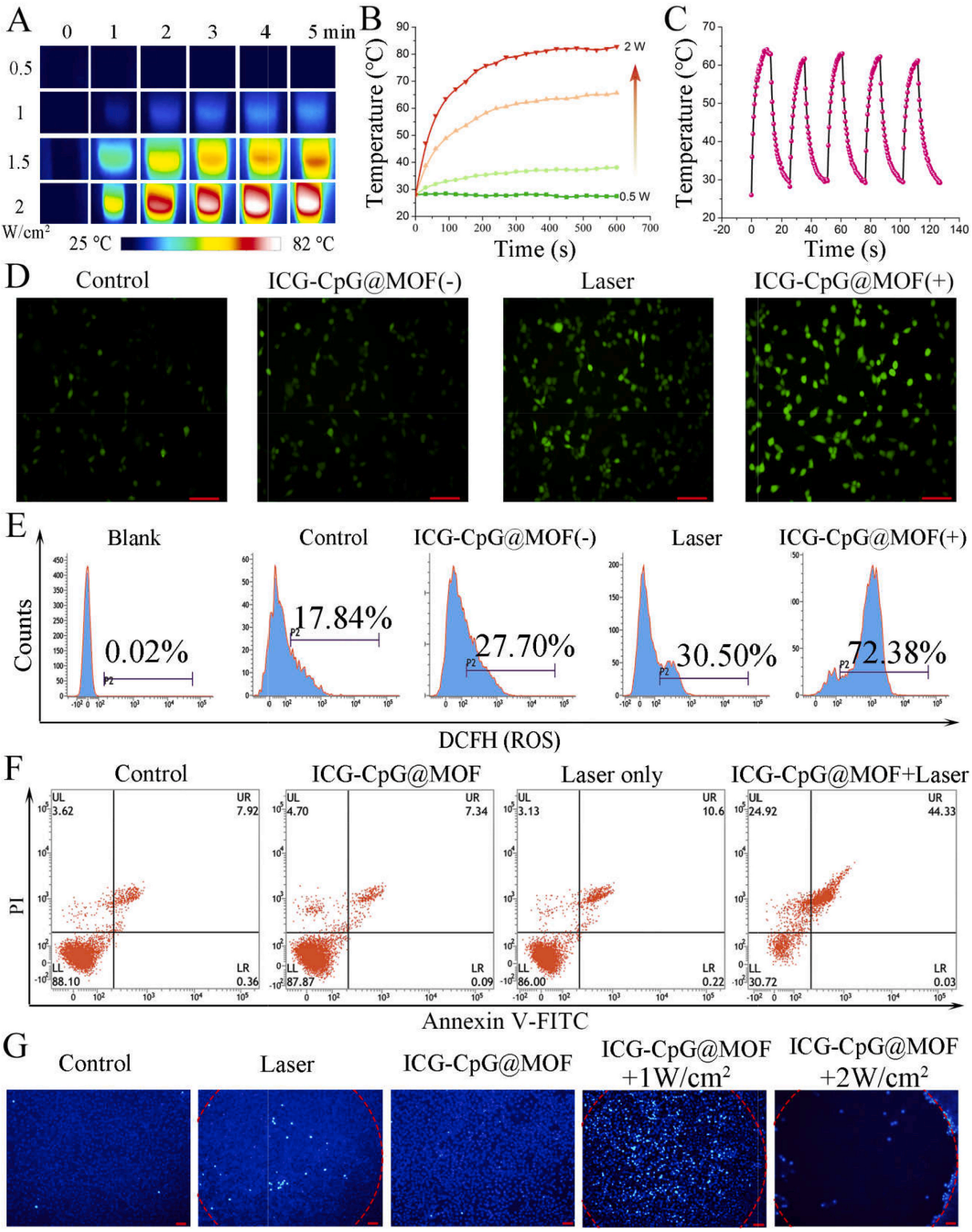

Fig. 3. Photothermal and photodynamic effects of ICG-CpG@MOF. A. Temperature images of ICG-CpG@MOF at different optical densities. Images of cells under irradiation from a 808 nm laser at a concentration of 100 μg/mL were recorded by an IR camera. **B.** Temperature elevation of the ICG-CpG@MOF solution (1 mL) at different densities by 808 nm light in aqueous solution. **C.** Photothermal conversion stability of ICG-CpG@MOF (100 μg/mL). The laser was turned on/turned off for five cycles (808 nm, 1.5 W/cm^2). **D.** Evaluation of ROS levels with a fluorescence microscope. Scale bar: 90 μm. **E.** Evaluation of ROS level with flow cytometry. **F.** Flow cytometry was used to detect the effect of ICG-CpG@MOF on cell death. **G.** Effect of ICG-CpG@MOF on cell death with Hoechst fluorescence staining. Scale bar: 90 μm. (D-E: The irradiation time was 5 min).

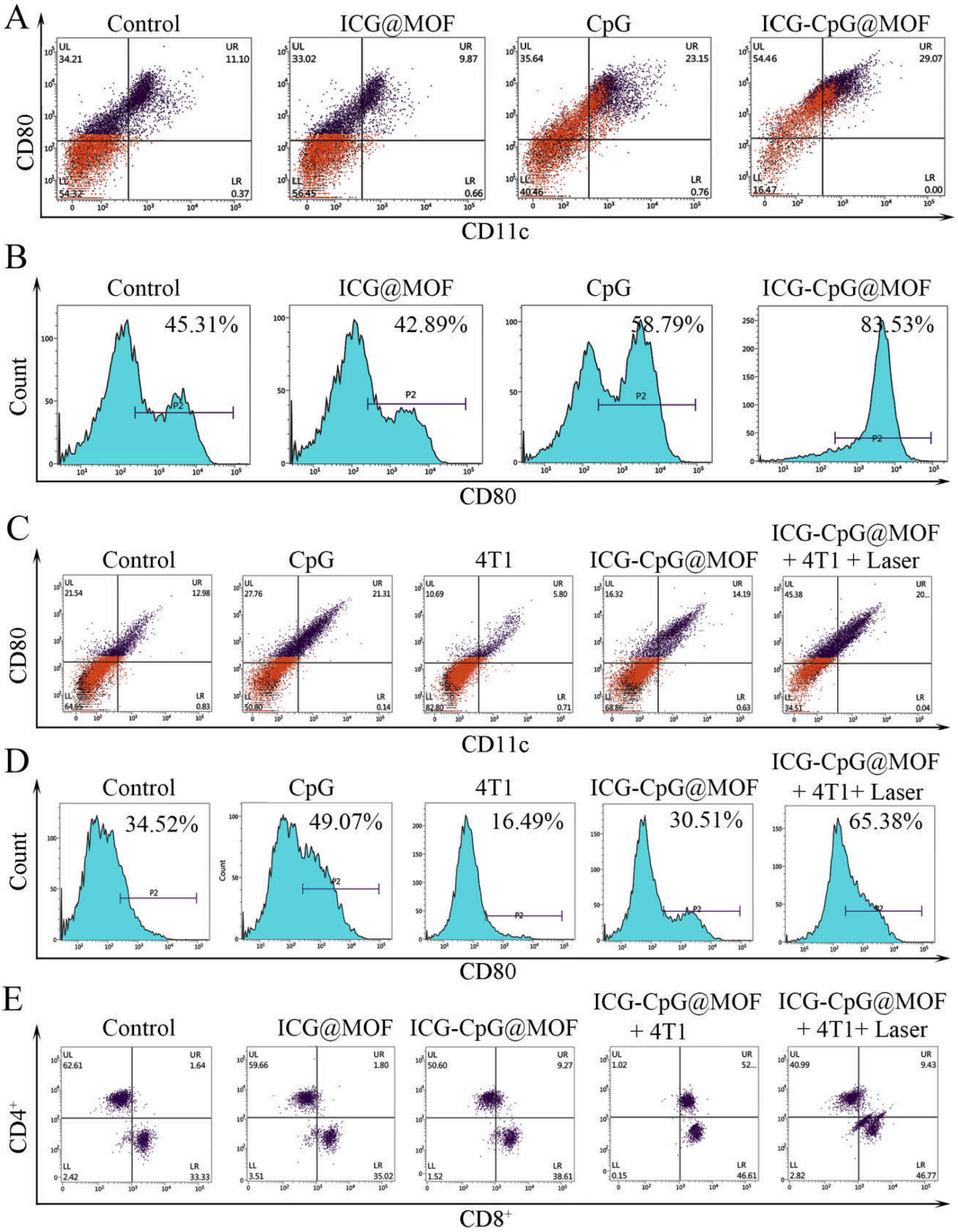

Fig. 4. Effect of ICG-CpG@MOF on the differentiation of immune cells. A. Regulatory effect of the ICG-CpG@MOF on peritoneal macrophages. Peritoneal macrophages were stained with PE-Cy7-anti-CD80 and FITC-anti-CD11c antibodies for flow cytometry. **B.** CD80 expression analysis of peritoneal macrophages**. C.** Regulatory effect of the ICG-CpG@MOF on adherent splenic cells. Cells were stained with a PE-Cy7-anti-CD80 and FITC-anti-CD11c antibodies for flow cytometry. **D.** CD80 expression analysis of adherent splenic cells**. E.** Effects of photothermal therapy on CD4 and CD8 expression in splenic T cells.

spleen began to show fluorescence signal, and it soon decreased. The tumor showed obvious fluorescence signal at 3 h, and the fluorescence gradually increased with the increase of time, reaching the maximum at 24 h. Magnetic resonance imaging (MRI) is a noninvasive imaging technique widely used in clinical medicine. ICG-CpG@MOF can be reduced by reducing agents such as GSH *in vivo*, thereby releasing ferrous ions, which can be used for MRI of tumors. With increasing MIL101-NH_2 concentration, the T2-weighted MRI images of ICG-CPG@MOF

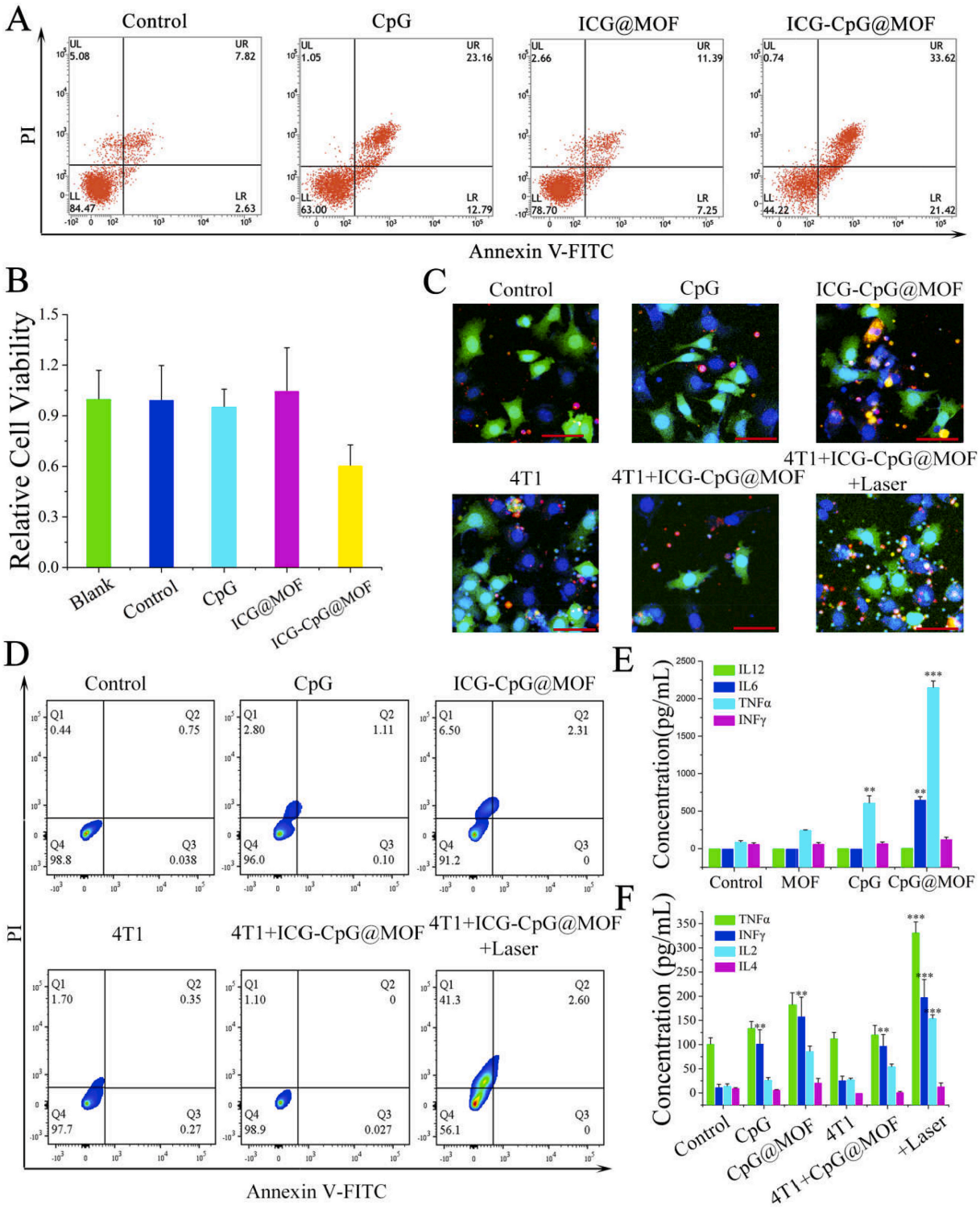

Fig. 5. Immunotherapeutic effect of ICG-CpG@MOF. A. The inhibitory effect of stimulated macrophages on tumor cells was determined by flow cytometry. **B.** Effect of the supernatant on tumor cell activity after differentiation of macrophages. **C.** Recognition of tumor cells by T cells after induction. Scale bar: 50 μm. **D.** Flow cytometry was used to detect photothermal residue induced T cell killing of tumor cells. **E.** ELISA was used to detect the production of immune factors after co-incubated with peritoneal macrophages for 48 h. **F.** ELISA was used to detect the production of immune factors after co-incubated with splenic lymphocytes for 72 h (**$p < 0.01$, ***$p < 0.001$.)

nanoparticles became darker (Fig. S17). As shown in Fig. 6B, ICG-CpG@MOF could significantly improve the imaging effect of MRI at tumor sites. Photothermal imaging for tumors was also obtained by infrared thermal imager (Fig. 6C). After ICG-CpG@MOF is enriched into tumor tissues through EPR effect, tumor tissues generate a large amount of heat during light irradiation, which can be detected by thermal imager. The experimental results show that the material has good photothermal treatment effect *in vivo*. Furthermore, ICG could serve as an effective photoacoustic contrast agent. Therefore, ICG-CpG@MOF can be used for photoacoustic imaging. As shown in Fig. 6D, a

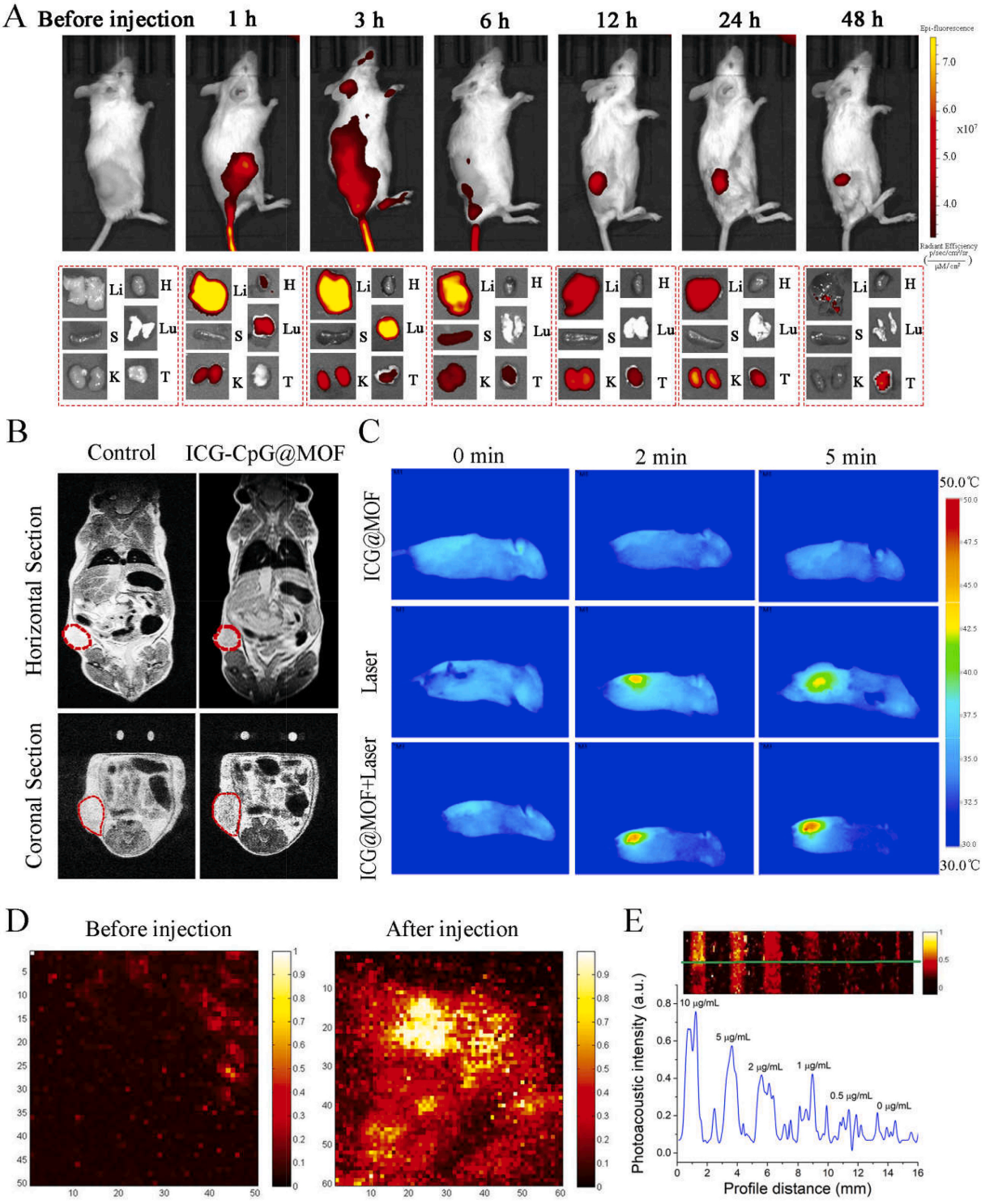

Fig. 6. Multimode imaging effect of ICG-CpG@MOF.A. Time series of the tumor near-infrared fluorescence imaging in situ and in organs after tail vein injection for 0 h–48 h. Li: Liver, H: Heart, S: Spleen, Lu: Lung, K: Kidney, T: Tumor. **B.** Horizontal section and coronal section nuclear magnetic imaging in tumor-bearing mice 2 h after in-situ injection. **C.** In situ photothermal imaging. **D.** Photoacoustic imaging of tumor before and after in situ injection. **E.** In vitro PA images of ICG-CpG@MOF solutions at different concentrations (0, 0.5, 1, 2, 5, and 10 μg/mL respectively).

photoacoustic signal was detected at the tumor site 6 h after tail vein injection. Strong photoacoustic signals were found after injection. The relationship between signal strength and concentration is shown in Fig. 6E. The above results indicate that the ICG-CpG@MOF has an effective passive tumor-targeting effect. This may be attributed to the EPR effect at tumor sites and the size of the MOF. Meanwhile, thanks to the multi-model imaging results of fluorescence, photoacoustic, photothermal, and nuclear magnetic resonance imaging, 6 h is selected as the best administration time for follow-up tumor therapy.

2.7. Therapeutic effect of the materials on tumor-bearing mice

Subcutaneous tumor-bearing mice were constructed from 4T1 cells. When the tumor diameter was approximately 5 mm, different

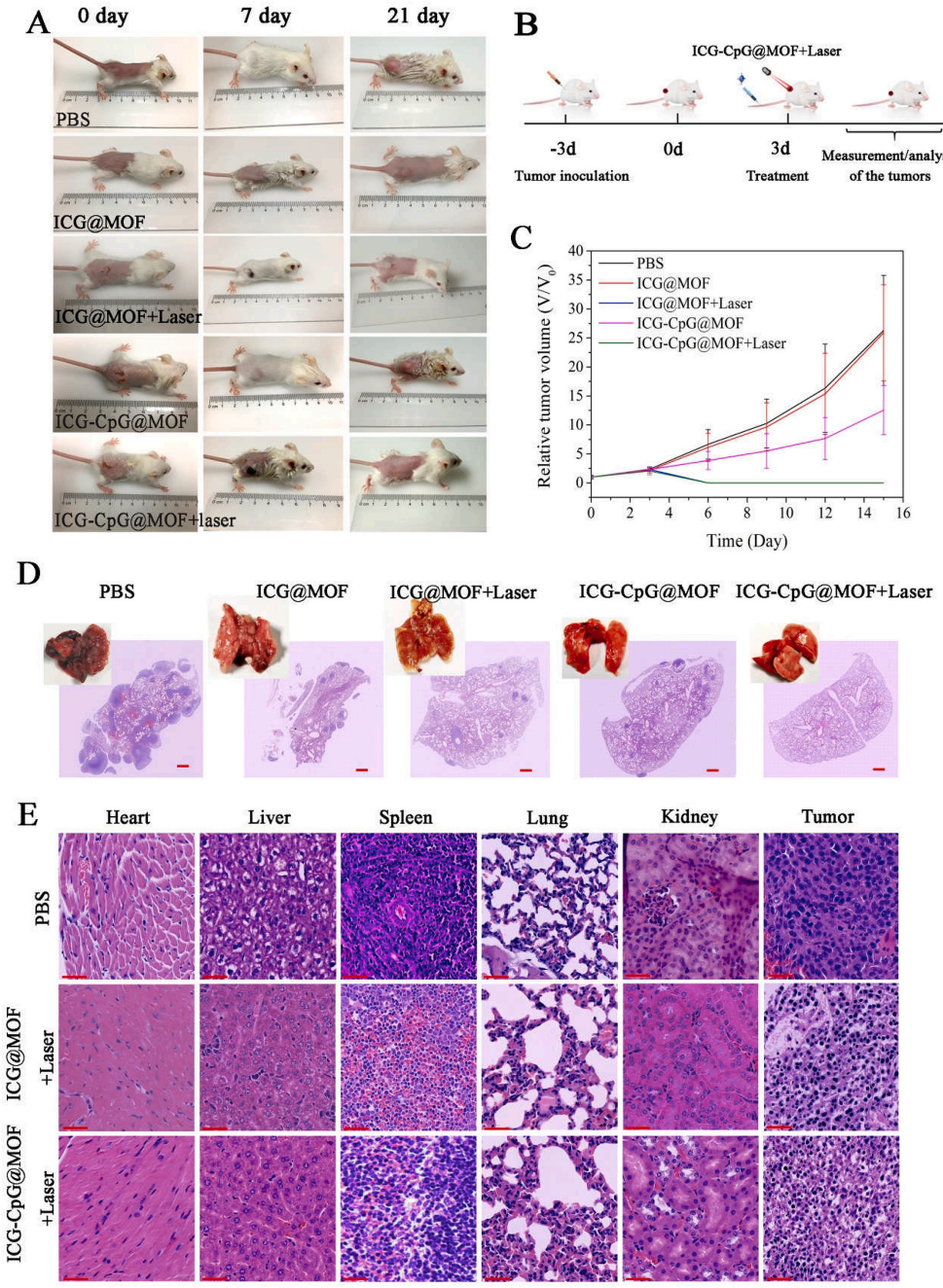

Fig. 7. In vivo therapeutic effect of ICG-CpG@MOF. A. Tumor volume change before and after treatment. **B.** The schematic outline shows the in *vivo* experimental design for treatments. **C.** Statistical analysis of tumor volume. **D.** The therapeutic effect of lung metastasis. **E.** H&E stained images of tumor and organs collected from the tumor bearing mice after various treatments. Scale bar: 90 μm.

treatments were used and tumor size was recorded. As shown in Fig. 7A, there was no statistically significant difference between the mice in different groups on day 0. Skin lesions appeared in the ICG-CpG@MOF + Laser group on day 7, and the lesions were basically repaired, with disappearance of the tumor on day 21. The statistical curve of tumor volume is shown in Fig. 7B. The survival rates of the mice in each group are presented in Fig. S18. The average survival times of the micetreated with PBS and ICG-CpG@MOF were 25.8 and 31.5 days, respectively. Significantly more mice treated with ICG-CpG@MOF + laser survived to the end of the study. We also constructed a lung metastasis model of breast cancer using 4T1 cells to detect the therapeutic effect on metastatic tumors. At 21 days after injection of 10^4 cells into the tail vein, the cancer cells in the control group infiltrated into the entire lung tissue, while the infiltration of the cancer cells in the treatment group was significantly inhibited (Fig. 7C). To test the histocompatibility of the MOF and its effect on various organs, hematoxylin and eosin (H&E) staining was performed for pathological examination after tumor-bearing mice were treated with ICG-CpG@MOF and irradiated with a pulse laser. As shown in Figs. 7D and S19, compared with that of the control group, the tumor tissues of the experimental group was edematous and vacuolated, while the H&E stained organs showed no obvious lesions, suggesting a reasonable and safe range of use. Since ICG-CpG@MOF is mainly distributed at sites in the liver and kidney, we examined indicators of liver and kidney injury. The ALT/AST results are shown in Fig. S20. The uric acid results are shown in Fig. S21. These results showed that MOF causes no obvious

damage to the body. Pharmacokinetic analysis was also performed, and the experimental results were shown in Fig. S22 and Table S1. After intravenous injection of ICG-CpG@MOF, the iron content in blood reaches the maximum value and decreases with the increase of time. About 15 h after the injection, iron levels in the blood were reduced to half of what they were at 1 h. The above experimental results show that ICG-CpG@MOF has good biodegradable activity and can be quickly removed by the body.

3. Conclusions

In summary, we constructed a multimodal imaging-guided synergistic cancer photoimmunotherapy by employing a specific MOF (MIL101-NH_2) as the core carrier; this MOF was dual-dressed with photoacoustic and fluorescent signal donors ICG and immune adjuvants CpG ODN and named ICG-CpG@MOF. This nanocarrier can passively target the tumor site through the EPR effect, achieving multimodal imaging (fluorescence, photoacoustic, photothermal and MR imaging) of the tumor, and light-actuated tumor therapies including photodynamic and photothermal methods, were simultaneously achieved with 808 nm laser irradiation. ICG-CpG@MOF facilitates the GSH-controlled release of immunoadjuvant into the tumor microenvironment. Furthermore, the released tumor-associated antigen along with CpG could activate the immune system, which significantly enhanced tumor cytotoxicity and achieved high cure rates with minimal side effects. This strategy utilizing multimodal imaging and synergistic cancer photoimmunotherapy provides a promising strategy for the diagnosis and treatment of cancer.

4. Experimental section

4.1. Materials

DAPI, FITC-CD3 antibody, APC-CD4 antibody, V450-CD8 antibody, PE-Cy7-CD80 antibody, and FITC-CD11C were obtained from Sigma. ROS Assay Kit and Hoechst fluorescent dye were purchased from Beijing Beyotime Biotechnology. CpG ODN (5′-TCC ATG ACG TTC CTG ACG TT-3′) was synthesized by BGI (Shenzhen, China). TRITC Phalloidin was purchased from Solarbio (CA1610). Annexin V-FITC/PI Apoptosis Detection Kit and CCK-8 (Cell Counting Kit-8) were purchased from Japan Dojindo Laboratories. All ELISA kits were obtained from Dakewe Bio-engineering Co., LTD (Shenzhen, China).

4.2. Animals and cells

The mouse breast cancer cell line 4T1 cells were obtained from the Cell bank of the Animal Experiment Center of Sun Yat-sen University. The peritoneal macrophage is acquired by the peritoneal lavatory as we did before [46]. Spleen lymphocytes were isolated as previously reported [49]. All the cells were cultured in DMEM or 1640 with 10% FBS (GIBCO, USA) in 37 ˚C incubator in 5% CO_2. 4–5 weeks old female Balb/c mice were obtained from Laboratory Animal Center of Southern Medical University. All animal experiments were approved by Southern Medical University's Institutional Animal Care and Use Committee.

4.3. Synthesis of MIL101-NH_2 (MOF)

The synthesis of MIL101-$NH_2$was consistent with that reported in previous literature [50]. In short, 2.07 mmol 2-aminoterephthalic acid and 4.16 mmol $FeCl_3{\cdot}6H_2O$ were dissolved in 30 mL DMF. After being treated at 120 ˚C for 20 h, the brown powder was centrifuged at 8500 rpm for 10 min and washed three times in turn with DMF. At last, the sediment was resuspended in DMF and stored at 4 ˚C.

4.4. Construction of ICG-CpG@MOF

This part of experimental methods refer to the previous published articles [51–53].1 μmol EDC and 1 μmol NHS were added to the solution of ICG-COOH (10 mM, 200 μL) to activate the eCOOH, and the mixture was thoroughly incorporated. MIL101-NH_2 (10 mg/mL, 1 mL) was then added. After 24 h of stir, the reactants (denoted as ICG@MOF) was recycled by centrifugation (8500 rpm, 10 min) and the supernatant was collected to determinate the content of free ICG by fluorescence quantitative. CpG ODN (65 μg) was dissolved in a certain amount of ultrapure water. 1 mg ICG@MOF was added and under magnetic stirring for 6 h. The collection denoted as ICG-CpG@MOF, and the supernatant was analyzed by a Nanodrop.

4.5. Characterization

The characterization method is a slight modification of what we have reported in our previous articles [54]. The MOF was diluted with ultra-pure water and dropped directly onto the copper network for TEM observation and elemental mappings. The MOF was diluted with ultrapure water and then dropped into the conductive glass and dried and sprayed with gold for scanning electron microscope observation. The zeta potentials and particle size of MOF nanoparticles were detected by Malvern Nano ZS90. Fourier transforms infrared (FT-IR) spectra of functionalized MOF were obtained by an Spectrum 400FT-IR spectrophotometer (PerkinElmer, USA), as reported previously [55]. Lambda 900 spectrophotometer (PerkinElmer, USA) was used to measure the UV–Vis absorption spectra of ICG-CpG@MOF. FL-8500 fluorescence spectrophotometer (PerkinElmer, USA) was used to record the fluorescence excitation and emission spectra of ICG-CpG@MOF, as we reported earlier [46]. A Nikon confocal laser scanning microscope was used to observe the internalization of fluorescently labeled MOF with a slight change from previous article [56]. The photothermal effects of ICG-CpG@MOF were evaluated using reported methods [57,58].

4.6. Toxicity tests in vitro and in vivo

The in vitro cell viability was detected by CCK-8 assay as previously reported [59]. In short, 4000 cells per well were incubated in a 96-well plate overnight. Different concentrations of ICG-CpG@MOF were added to the medium. Then the cells were incubated for another 24 h. Finally, the relative cell viability was detected by CCK-8 assay. In vivo toxicity was explored by organ functions detection and histopathological study from mice in different treatment groups. 100 μL PBS or suspension of ICG-CpG@MOF (150 μg) in PBS were intravenously injected into mice. Blood was collected at 48 h. Liver (ALT and AST) and kidney (Uric acid) functions were tested by Shenzhen Third People's Hospital (Shenzhen, China). After treatment, mice were sacrificed to collect main organs and tumors.

4.7. Measurement of immune system activation and expression of cytokines

Peritoneal macrophages and splenocytes (2.5×10^6 cells/mL) were stimulated according to the requirements of the article. For example, T cells were stimulated with 4T1 cell residue after photothermal ablation (60 μg/mL, protein quantification) for 60 h. Macrophages were incubated with ICG-CpG@MOF for 48 h. After centrifugation, the medium was collected and used to detect cytokine levels by ELISA. The cells were stained with FITC-anti-CD3e, V450-anti-CD8α, APC-anti-CD4, FITC-anti-CD11c or PE-cy7-anti-CD80 according to the need. At last, the treated cells were examined by a flow cytometer.

4.8. Cell apoptosis assay

Apoptosis assay was performed via a method described in the manufacturer with slight modification (Flow Cytometry Apoptosis

Detection Kit). In short, cells were collected after being washed with PBS, re-suspended in 500 μL of binding buffer, and incubated with each 5 μL of FITC-Annexin V and PI in the dark for 15 min in 25 °C. Then they were evaluated by flow cytometry (BD FACSVerse, BD Biosciences, USA). Hoechst staining was performed using the reported method [60]. In short, the cells to be tested were washed with PBS for two to three times and stained with the diluted dye for no more than 5 min, then the dye was removed and washed with PBS for two to three times, and the cells were observed using an Olympus microscope (Olympus FV1000, Japan).

4.9. Animal imaging experiments

Multimodal imaging experiments were performed as previously described with a simple modification. Near-infrared fluorescence imaging was performed using IVIS Spectrum with a ICG channel [61]. IVPAT system was used in the photoacoustic imaging experiment [62]. The NMR imaging experiment referred to the previously reported methods [42]. The amount of ICG-CpG@MOF used for intravenously injection was 0.15 mg per mouse.

4.10. Tumor model construction and immunization studies

The Bal b/c mice were randomly divided into five groups (each group containing 5 mice). In the beginning, tumors were formed by subcutaneous implantation of 10^6 4T1 cells. When the tumor volume had grown to about 60 mm^3, 100 μL of PBS, CpG, ICG@MOF, and ICG-CpG@MOF with equivalent doses (about 4.5 μg of CpG ODN) were injected intravenously into the mice. Then, multimodal imaging was observed and directed 808 nm laser irradiation was given. Tumor volume and survival were then calculated. In order to detect the immune effect, drugs were injected into the tail vein when the tumor volume reached 60 mm^3, and laser irradiation treatment was given according to the above methods. Three days after the experiment, 10^4 4T1 cells were injected into the caudal vein to simulate tumor metastasis. On day 21, the mice were anesthetized and sacrificed and lungs were removed for subsequent analysis.

4.11. H&E staining

H&E staining was performed as previously described [63]. After the mice were euthanized, tumors tissues and visceral organs were collected. The organs and tissues were fixed in 4% formaldehyde overnight. Before H&E staining, Paraffin embedding and slicing is required. Finally, all slices analyzed using Motic Easy Scan (Motic Asia, China).

4.12. Statistical analysis

The data from one representative experiment among at least three independent experiments are expressed as the mean ± SEM. Unless otherwise stated, statistical analysis was performed with Student's paired *t*-test using SPSS software (SPSS Inc., Chicago, IL, USA), and the differences were considered to be statistically significant at $p < 0.05$. Kaplan-Meier survival analyses were performed to analyze the survival rate of mice after tumor-bearing.

CRediT authorship contribution statement

Zhijin Fan: Conceptualization, Methodology, Software, Data curation, Writing - original draft. **Hongxing Liu:** Visualization, Methodology, Data curation, Writing - original draft. **Yaohua Xue:** Resources, Supervision. **Jingyan Lin:** Methodology, Software, Data curation. **Yu Fu:** Visualization. **Zhaohua Xia:** Software, Methodology. **Dongming Pan:** Methodology. **Jian Zhang:** Methodology, Writing - review & editing. **Kun Qiao:** Funding acquisition, Writing - review & editing. **Zhenzhen Zhang:** Funding acquisition, Writing - review & editing. **Yuhui Liao:** Writing - review & editing, Supervision, Funding acquisition, Project administration.

Declaration of competing interest

There is no conflict of interest.

Acknowledgment

This work was supported by grants from the National Natural Science Foundation of China, China (21904145, 81972019 and 31700150), China Postdoctoral Science Foundation, China (2018M633273), Chen Jingyu team of Sanming Project of Medicine in Shenzhen, China (SZSM201812058), Guangdong Provincial Science and Technology Plan project, China (No.2017B030314108).

Abbreviations

MOFs	metal-organic frameworks
ICG	Indocyanine green
CpG	Cytosine-phosphate-guanine sequence
EPR	enhanced permeability and retention effect
MRI	Magnetic resonance imaging
PDT	photodynamic therapy
PTT	photothermal therapy
GSH	glutathione

References

[1] F. Bray, J. Ferlay, I. Soerjomataram, R.L. Siegel, L.A. Torre, A. Jemal, Global cancer statistics 2018: GLOBOCAN estimates of incidence and mortality worldwide for 36 cancers in 185 countries, Ca - Cancer J. Clin. 68 (6) (2018) 394–424, https://doi.org/10.3322/caac.21492.

[2] R.L. Anderson, T. Balasas, J. Callaghan, R.C. Coombes, J. Evans, J.A. Hall, S. Kinrade, D. Jones, P.S. Jones, R. Jones, J.F. Marshall, M.B. Panico, J.A. Shaw, P.S. Steeg, M. Sullivan, W. Tong, A.D. Westwell, J.W.A. RitchieU.K. Cancer Research, C.R.C.A.M.W.G. Cancer Therapeutics, A framework for the development of effective anti-metastatic agents, Nat. Rev. Clin. Oncol. 16 (3) (2019) 185–204, https://doi.org/10.1038/s41571-018-0134-8.

[3] K.D. Miller, R.L. Siegel, C.C. Lin, A.B. Mariotto, J.L. Kramer, J.H. Rowland, K.D. Stein, R. Alteri, A. Jemal, Cancer treatment and survivorship statistics, 2016, Ca - Cancer J. Clin. 66 (4) (2016) 271–289, https://doi.org/10.3322/caac.21349.

[4] D. Fukumura, J. Kloepper, Z. Amoozgar, D.G. Duda, R.K. Jain, Enhancing cancer immunotherapy using antiangiogenics: opportunities and challenges, Nat. Rev. Clin. Oncol. 15 (5) (2018) 325–340, https://doi.org/10.1038/nrclinonc.2018.29.

[5] I. Mellman, G. Coukos, G. Dranoff, Cancer immunotherapy comes of age, Nature 480 (7378) (2011) 480–489, https://doi.org/10.1038/nature10673.

[6] D. Wang, T. Wang, J. Liu, H. Yu, S. Jiao, B. Feng, F. Zhou, Y. Fu, Q. Yin, P. Zhang, Z. Zhang, Z. Zhou, Y. Li, Acid-activatable versatile micelleplexes for PD-L1 blockade-enhanced cancer photodynamic immunotherapy, Nano Lett. 16 (9) (2016) 5503–5513, https://doi.org/10.1021/acs.nanolett.6b01994.

[7] M. Wu, D. Zheng, D. Zhang, P. Yu, L. Peng, F. Chen, Z. Lin, Z. Cai, J. Li, Z. Wei, X. Lin, J. Liu, X. Liu, Converting immune cold into hot by biosynthetic functional vesicles to boost systematic antitumor immunity, iScience 23 (7) (2020), https://doi.org/10.1016/j.isci.2020.101341.

[8] C. Zhang, P. Oberoi, S. Oelsner, A. Waldmann, A. Lindner, T. Tonn, W.S. Wels, Chimeric antigen receptor-engineered NK-92 cells: an off-the-shelf cellular therapeutic for targeted elimination of cancer cells and induction of protective anti-tumor immunity, Front. Immunol. 8 (2017) 533, https://doi.org/10.3389/fimmu.2017.00533.

[9] Y. Li, J. Lin, Z. Cai, P. Wang, Q. Luo, C. Yao, Y. Zhang, Z. Hou, J. Liu, X. Liu, Tumor microenvironment-activated self-recognizing nanodrug through directly tailored assembly of small-molecules for targeted synergistic chemotherapy, J. Contr. Release 321 (2020) 222–235, https://doi.org/10.1016/j.jconrel.2020.02.025.

[10] Y. Li, J. Lin, P. Wang, Q. Luo, H. Lin, Y. Zhang, Z. Hou, J. Liu, X. Liu, Tumor microenvironment responsive shape-reversal self-targeting virus-inspired nanodrug for imaging-guided near-infrared-II photothermal chemotherapy, ACS Nano 13 (11) (2019) 12912–12928, https://doi.org/10.1021/acsnano.9b05425.

[11] G.B. Kim, V. Aragon-Sanabria, L. Randolph, H. Jiang, J.A. Reynolds, B.S. Webb, A. Madhankumar, X. Lian, J.R. Connor, J. Yang, C. Dong, High-affinity mutant Interleukin-13 targeted CAR T cells enhance delivery of clickable biodegradable fluorescent nanoparticles to glioblastoma, Bioact Mater 5 (3) (2020) 624–635, https://doi.org/10.1016/j.bioactmat.2020.04.011.

[12] D. Zhang, Y. Zheng, Z. Lin, X. Liu, J. Li, H. Yang, W. Tan, Equipping natural killer cells with specific targeting and checkpoint blocking aptamers for enhanced adoptive immunotherapy in solid tumors, Angew Chem. Int. Ed. Engl. 59 (29)

(2020) 12022–12028, https://doi.org/10.1002/anie.202002145.
[13] J.L. Benci, B. Xu, Y. Qiu, T.J. Wu, H. Dada, C. Twyman-Saint Victor, L. Cucolo, D.S.M. Lee, K.E. Pauken, A.C. Huang, T.C. Gangadhar, R.K. Amaravadi, L.M. Schuchter, M.D. Feldman, H. Ishwaran, R.H. Vonderheide, A. Maity, E.J. Wherry, A.J. Minn, Tumor interferon signaling regulates a multigenic resistance program to immune checkpoint blockade, Cell 167 (6) (2016) 1540–1554, https://doi.org/10.1016/j.cell.2016.11.022 e12.
[14] N. McGranahan, A.J. Furness, R. Rosenthal, S. Ramskov, R. Lyngaa, S.K. Saini, M. Jamal-Hanjani, G.A. Wilson, N.J. Birkbak, C.T. Hiley, T.B. Watkins, S. Shafi, N. Murugaesu, R. Mitter, A.U. Akarca, J. Linares, T. Marafioti, J.Y. Henry, E.M. Van Allen, D. Miao, B. Schilling, D. Schadendorf, L.A. Garraway, V. Makarov, N.A. Rizvi, A. Snyder, M.D. Hellmann, T. Merghoub, J.D. Wolchok, S.A. Shukla, C.J. Wu, K.S. Peggs, T.A. Chan, S.R. Hadrup, S.A. Quezada, C. Swanton, Clonal neoantigens elicit T cell immunoreactivity and sensitivity to immune checkpoint blockade, Science 351 (6280) (2016) 1463–1469, https://doi.org/10.1126/science.aaf1490.
[15] S.L. Topalian, J.M. Taube, R.A. Anders, D.M. Pardoll, Mechanism-driven biomarkers to guide immune checkpoint blockade in cancer therapy, Nat. Rev. Canc. 16 (5) (2016) 275–287, https://doi.org/10.1038/nrc.2016.36.
[16] C. Ainsworth, Building a better lymphoma vaccine, Nature 563 (7731) (2018) S52–S54, https://doi.org/10.1038/d41586-018-07366-1.
[17] E. Bender, Cancer immunotherapy, S61, Nature 552 (7685) (2017), https://doi.org/10.1038/d41586-017-08699-z.
[18] N. van Montfoort, L. Borst, M.J. Korrer, M. Sluijter, K.A. Marijt, S.J. Santegoets, V.J. van Ham, I. Ehsan, P. Charoentong, P. Andre, N. Wagtmann, M.J.P. Welters, Y.J. Kim, S.J. Piersma, S.H. van der Burg, T. van Hall, NKG2A blockade potentiates CD8 T cell immunity induced by cancer vaccines, Cell 175 (7) (2018) 1744–1755, https://doi.org/10.1016/j.cell.2018.10.028 e15.
[19] Z. Li, Y. Hu, Q. Fu, Y. Liu, J. Wang, J. Song, H. Yang, NIR/ROS-Responsive black phosphorus QD vesicles as immunoadjuvant carrier for specific cancer photodynamic immunotherapy, Adv. Funct. Mater. 30 (3) (2019) 1905758, https://doi.org/10.1002/adfm.201905758.
[20] H. Zhao, J. Xu, Y. Li, X. Guan, X. Han, Y. Xu, H. Zhou, R. Peng, J. Wang, Z. Liu, Nanoscale coordination polymer based nanovaccine for tumor immunotherapy, ACS Nano 13 (11) (2019) 13127–13135, https://doi.org/10.1021/acsnano.9b05974.
[21] L. Chen, L. Zhou, C. Wang, Y. Han, Y. Lu, J. Liu, X. Hu, T. Yao, Y. Lin, S. Liang, S. Shi, C. Dong, Tumor-targeted drug and CpG delivery system for phototherapy and docetaxel-enhanced immunotherapy with polarization toward M1-type macrophages on triple negative breast cancers, Adv. Mater. 31 (52) (2019) e1904997, , https://doi.org/10.1002/adma.201904997.
[22] J. Chen, C. Liang, X. Song, X. Yi, K. Yang, L. Feng, Z. Liu, Hybrid protein nanoreactors enable simultaneous increments of tumor oxygenation and iodine-131 delivery for enhanced radionuclide therapy, Small 15 (46) (2019) e1903628, , https://doi.org/10.1002/smll.201903628.
[23] C.W. Ng, J. Li, K. Pu, Recent progresses in phototherapy-synergized cancer immunotherapy, Adv. Funct. Mater. 28 (46) (2018) 1804688, , https://doi.org/10.1002/adfm.201804688.
[24] S. Ma, W. Song, Y. Xu, X. Si, S. Lv, Y. Zhang, Z. Tang, X. Chen, Rationally designed polymer conjugate for tumor-specific amplification of oxidative stress and boosting antitumor immunity, Nano Lett. 20 (4) (2020) 2514–2521, https://doi.org/10.1021/acs.nanolett.9b05265.
[25] L. Zheng, X. Hu, H. Wu, L. Mo, S. Xie, J. Li, C. Peng, S. Xu, L. Qiu, W. Tan, In vivo monocyte/macrophage-hitchhiked intratumoral accumulation of nanomedicines for enhanced tumor therapy, J. Am. Chem. Soc. 142 (1) (2020) 382–391, https://doi.org/10.1021/jacs.9b11046.
[26] R. Ge, C. Liu, X. Zhang, W. Wang, B. Li, J. Liu, Y. Liu, H. Sun, D. Zhang, Y. Hou, H. Zhang, B. Yang, Photothermal-activatable Fe3O4 superparticle nanodrug carriers with PD-L1 immune checkpoint blockade for anti-metastatic cancer immunotherapy, ACS Appl. Mater. Interfaces 10 (24) (2018) 20342–20355, https://doi.org/10.1021/acsami.8b05876.
[27] D. Wu, Y. Yu, C. Zhao, X. Shou, Y. Piao, X. Zhao, Y. Zhao, S. Wang, NK-Cell-Encapsulated porous microspheres via microfluidic electrospray for tumor immunotherapy, ACS Appl. Mater. Interfaces 11 (37) (2019) 33716–33724, https://doi.org/10.1021/acsami.9b12816.
[28] W. Song, M. Das, X. Chen, Nanotherapeutics for immuno-oncology: a crossroad for new paradigms, Trends Cancer 6 (4) (2020) 288–298, https://doi.org/10.1016/j.trecan.2020.01.011.
[29] J. Nam, S. Son, K.S. Park, W. Zou, L.D. Shea, J.J. Moon, Cancer nanomedicine for combination cancer immunotherapy, Nat. Rev. Mater. 4 (6) (2019) 398–414, https://doi.org/10.1038/s41578-019-0108-1.
[30] J. Liu, R. Zhang, Z.P. Xu, Nanoparticle-based nanomedicines to promote cancer immunotherapy: recent advances and future directions, Small 15 (32) (2019) e1900262, , https://doi.org/10.1002/smll.201900262.
[31] Y. Wang, W. Wu, J. Liu, P.N. Manghnani, F. Hu, D. Ma, C. Teh, B. Wang, B. Liu, Cancer-cell-activated photodynamic therapy assisted by Cu(II)-Based metal-organic framework, ACS Nano 13 (6) (2019) 6879–6890, https://doi.org/10.1021/acsnano.9b01665.
[32] S.S. Wan, Q. Cheng, X. Zeng, X.Z. Zhang, A Mn(III)-Sealed metal-organic framework nanosystem for redox-unlocked tumor theranostics, ACS Nano 13 (6) (2019) 6561–6571, https://doi.org/10.1021/acsnano.9b00300.
[33] D. Wang, H. Wu, W.Q. Lim, S.Z.F. Phua, P. Xu, Q. Chen, Z. Guo, Y. Zhao, A mesoporous nanoenzyme derived from metal-organic frameworks with endogenous oxygen generation to alleviate tumor hypoxia for significantly enhanced photodynamic therapy, Adv. Mater. 31 (27) (2019) e1901893, , https://doi.org/10.1002/adma.201901893.
[34] K. Lu, T. Aung, N. Guo, R. Weichselbaum, W. Lin, Nanoscale metal-organic frameworks for therapeutic, imaging, and sensing applications, Adv. Mater. 30 (37) (2018) e1707634, , https://doi.org/10.1002/adma.201707634.
[35] L. Sun, Y. Xu, Y. Gao, X. Huang, S. Feng, J. Chen, X. Wang, L. Guo, M. Li, X. Meng, J. Zhang, J. Ge, X. An, D. Ding, Y. Luo, Y. Zhang, Q. Jiang, X. Ning, Synergistic amplification of oxidative stress-mediated antitumor activity via liposomal dichloroacetic acid and MOF-Fe(2), Small 15 (24) (2019) e1901156, , https://doi.org/10.1002/smll.201901156.
[36] K. Ni, T. Luo, G. Lan, A. Culbert, Y. Song, T. Wu, X. Jiang, W. Lin, A nanoscale metal-organic framework to mediate photodynamic therapy and deliver CpG oligodeoxynucleotides to enhance antigen presentation and cancer immunotherapy, Angew Chem. Int. Ed. Engl. 59 (3) (2020) 1108–1112, https://doi.org/10.1002/anie.201911429.
[37] L. Wang, X. Qu, Y. Zhao, Y. Weng, G.I.N. Waterhouse, H. Yan, S. Guan, S. Zhou, Exploiting single atom iron centers in a porphyrin-like MOF for efficient cancer phototherapy, ACS Appl. Mater. Interfaces 11 (38) (2019) 35228–35237, https://doi.org/10.1021/acsami.9b11238.
[38] Z. Dong, Y. Sun, J. Chu, X. Zhang, H. Deng, Multivariate metal-organic frameworks for dialing-in the binding and programming the release of drug molecules, J. Am. Chem. Soc. 139 (40) (2017) 14209–14216, https://doi.org/10.1021/jacs.7b07392.
[39] K.M. Taylor-Pashow, J. Della Rocca, Z. Xie, S. Tran, W. Lin, Postsynthetic modifications of iron-carboxylate nanoscale metal-organic frameworks for imaging and drug delivery, J. Am. Chem. Soc. 131 (40) (2009) 14261–14263, https://doi.org/10.1021/ja906198y.
[40] K. Ni, T. Luo, A. Culbert, M. Kaufmann, X. Jiang, W. Lin, Nanoscale metal-organic framework Co-delivers TLR-7 agonists and anti-CD47 antibodies to modulate macrophages and orchestrate cancer immunotherapy, J. Am. Chem. Soc. (2020), https://doi.org/10.1021/jacs.0c05039.
[41] W. Zhu, J. Zhao, Q. Chen, Z. Liu, Nanoscale metal-organic frameworks and coordination polymers as theranostic platforms for cancer treatment, Coord. Chem. Rev. 398 (2019), https://doi.org/10.1016/j.ccr.2019.07.006.
[42] Y. Zhang, C. Liu, F. Wang, Z. Liu, J. Ren, X. Qu, Metal-organic-framework-supported immunostimulatory oligonucleotides for enhanced immune response and imaging, Chem. Commun. 53 (11) (2017) 1840–1843, https://doi.org/10.1039/c6cc09280b.
[43] Y. Yang, Q. Chen, J.P. Wu, T.B. Kirk, J. Xu, Z. Liu, W. Xue, Reduction-responsive codelivery system based on a metal-organic framework for eliciting potent cellular immune response, ACS Appl. Mater. Interfaces 10 (15) (2018) 12463–12473, https://doi.org/10.1021/acsami.8b01680.
[44] C. Commisso, S.M. Davidson, R.G. Soydaner-Azeloglu, S.J. Parker, J.J. Kamphorst, S. Hackett, E. Grabocka, M. Nofal, J.A. Drebin, C.B. Thompson, J.D. Rabinowitz, C.M. Metallo, M.G. Vander Heiden, D. Bar-Sagi, Macropinocytosis of protein is an amino acid supply route in Ras-transformed cells, Nature 497 (7451) (2013) 633–637, https://doi.org/10.1038/nature12138.
[45] W. Li, J. Yang, L. Luo, M. Jiang, B. Qin, H. Yin, C. Zhu, X. Yuan, J. Zhang, Z. Luo, Y. Du, Q. Li, Y. Lou, Y. Qiu, J. You, Targeting photodynamic and photothermal therapy to the endoplasmic reticulum enhances immunogenic cancer cell death, Nat. Commun. 10 (1) (2019) 3349, https://doi.org/10.1038/s41467-019-11269-8.
[46] C. Lu, Z. Fan, D. Xing, Photo-enhancement of macrophage phagocytic activity via Rac1-mediated signaling pathway: implications for bacterial infection, Int. J. Biochem. Cell Biol. 78 (2016) 206–216, https://doi.org/10.1016/j.biocel.2016.06.010.
[47] N.G. Sosale, K.R. Spinler, C. Alvey, D.E. Discher, Macrophage engulfment of a cell or nanoparticle is regulated by unavoidable opsonization, a species-specific 'Marker of Self' CD47, and target physical properties, Curr. Opin. Immunol. 35 (2015) 107–112, https://doi.org/10.1016/j.coi.2015.06.013.
[48] Y.W. Choo, M. Kang, H.Y. Kim, J. Han, S. Kang, J.R. Lee, G.J. Jeong, S.P. Kwon, S.Y. Song, S. Go, M. Jung, J. Hong, B.S. Kim, M1 macrophage-derived nanovesicles potentiate the anticancer efficacy of immune checkpoint inhibitors, ACS Nano 12 (9) (2018) 8977–8993, https://doi.org/10.1021/acsnano.8b02446.
[49] H.C. Chang, Z.Z. Zou, Q.H. Wang, J. Li, H. Jin, Q.X. Yin, D. Xing, Targeting and specific activation of antigen-presenting cells by endogenous antigen-loaded nanoparticles elicits tumor-specific immunity, Adv. Sci. 7 (1) (2020) 1900069, https://doi.org/10.1002/advs.201900069.
[50] S. Bauer, C. Serre, T. Devic, P. Horcajada, J. Marrot, G. Ferey, N. Stock, High-throughput assisted rationalization of the formation of metal organic frameworks in the Iron(III) aminoterephthalate solvothermal system, Inorg. Chem. 47 (17) (2008) 7568–7576, https://doi.org/10.1021/ic800538r.
[51] C. Jiang, G. Wang, R. Hein, N. Liu, X. Luo, J.J. Davis, Antifouling strategies for selective in vitro and in vivo sensing, Chem. Rev. 120 (8) (2020) 3852–3889, https://doi.org/10.1021/acs.chemrev.9b00739.
[52] Z. Fan, J. Yu, J. Lin, Y. Liu, Y. Liao, Exosome-specific tumor diagnosis via biomedical analysis of exosome-containing microRNA biomarkers, Analyst 144 (19) (2019) 5856–5865, https://doi.org/10.1039/c9an00777f.
[53] H. Liu, W. Lin, L. He, T. Chen, Radiosensitive core/satellite ternary heteronanostructure for multimodal imaging-guided synergistic cancer radiotherapy, Biomaterials 226 (2020) 119545, https://doi.org/10.1016/j.biomaterials.2019.119545.
[54] Z. Fan, K. Xiao, J. Lin, Y. Liao, X. Huang, Functionalized DNA enables programming exosomes/vesicles for tumor imaging and therapy, Small 15 (47) (2019) e1903761, , https://doi.org/10.1002/smll.201903761.
[55] D. Zhang, Y. Zheng, Z. Lin, S. Lan, X. Zhang, A. Zheng, J. Li, G. Liu, H. Yang, X. Liu, J. Liu, Artificial engineered natural killer cells combined with antiheat endurance as a powerful strategy for enhancing photothermal-immunotherapy efficiency of solid tumors, Small 15 (42) (2019) e1902636, , https://doi.org/10.1002/smll.201902636.
[56] B. Shu, Z. Li, X. Yang, F. Xiao, D. Lin, X. Lei, B. Xu, D. Liu, Active droplet-array (ADA) microfluidics enables multiplexed complex bioassays for point of care

testing, Chem. Commun. 54 (18) (2018) 2232–2235, https://doi.org/10.1039/c7cc09377b.
[57] W. Huang, Y. Huang, Y. You, T. Nie, T. Chen, High-yield synthesis of multifunctional tellurium nanorods to achieve simultaneous chemo-photothermal combination cancer therapy, Adv. Funct. Mater. 27 (33) (2017), https://doi.org/10.1002/adfm.201701388.
[58] Y. Cheng, F. Yang, G. Xiang, K. Zhang, Y. Cao, D. Wang, H. Dong, X. Zhang, Ultrathin tellurium oxide/ammonium tungsten bronze nanoribbon for multimodality imaging and second near-infrared region photothermal therapy, Nano Lett. 19 (2) (2019) 1179–1189, https://doi.org/10.1021/acs.nanolett.8b04618.
[59] Q. Zhang, G. Kuang, S. He, H. Lu, Y. Cheng, D. Zhou, Y. Huang, Photoactivatable prodrug-backboned polymeric nanoparticles for efficient light-controlled gene delivery and synergistic treatment of platinum-resistant ovarian cancer, Nano Lett. (2020), https://doi.org/10.1021/acs.nanolett.9b04981.
[60] L. Wen, W. Ding, S. Yang, D. Xing, Microwave pumped high-efficient thermoacoustic tumor therapy with single wall carbon nanotubes, Biomaterials 75 (2016) 163–173, https://doi.org/10.1016/j.biomaterials.2015.10.028.
[61] Q. Zhang, S. He, G. Kuang, S. Liu, H. Lu, X. Li, D. Zhou, Y. Huang, Morphology tunable and acid-sensitive dextran-doxorubicin conjugate assemblies for targeted cancer therapy, J. Mater. Chem. B (2020), https://doi.org/10.1039/d0tb00746c.
[62] J. Zhang, S. Yang, X. Ji, Q. Zhou, D. Xing, Characterization of lipid-rich aortic plaques by intravascular photoacoustic tomography: ex vivo and in vivo validation in a rabbit atherosclerosis model with histologic correlation, J. Am. Coll. Cardiol. 64 (4) (2014) 385–390, https://doi.org/10.1016/j.jacc.2014.04.053.
[63] Y. Zang, Y. Wei, Y. Shi, Q. Chen, D. Xing, Chemo/photoacoustic dual therapy with mRNA-triggered DOX release and photoinduced shockwave based on a DNA-gold nanoplatform, Small 12 (6) (2016) 756–769, https://doi.org/10.1002/smll.201502857.